arXiv:2505.09158v1 [physics.optics] 14 May 2025

Spatial Offset of Excited States in Non-Hermitian Lattices

Xiaohan Jiang, Yuanyuan Pan, Yang Zhang, and Ye Xiong*
Institute of Theoretical Physics, Nanjing Normal University - Nanjing 210023, PRC

We investigate the behavior of light-wave packets injected into non-Hermitian microcavity lattices under highly dissipative conditions. While all eigenstates of the lattice exhibit exponential decay, a specifically excited state maintains coherent propagation. In a one-dimensional lattice, this state undergoes a spatial displacement shift away from the injection position, which is a fundamental property of non-Hermitian systems with a point gap when the spectrum encircles a finite region in the complex plane. Extending such a shift to two-dimensional lattices reveals a geometrically anomalous V-shaped wave packet formation with orientation-tunable arms. Notably, this geometric control mechanism enables all-optical steering of non-Hermitian photonic states without requiring structural modifications.

I. INTRODUCTIONS.

Non-Hermitian systems governed by complex Hamiltonians exhibit unique phenomena, including PT symmetry breaking[1–7], exceptional points[8–13], and generalized Brillouin zones[14–16]. These features fundamentally stem from the non-orthogonality between left and right eigenstates and the eigenspectrum in the complex plane. For example, eigenstates with positive imaginary eigenvalues (amplification) or negative imaginary eigenvalues (dissipation) exhibit asymmetric amplification profiles in time and space, inducing non-reciprocal transport in systems with non-reciprocal couplings or hoppings[17–25]. However, practical implementations face a fundamental stability dichotomy: systems with eigenspectral components above the real axis in the complex plane exhibit dynamical instability, while those with entirely sub-real-axis spectra suffer from global mode decay, rendering stable experimental observation unattainable[26].

In this study, we examine the response of a non-Hermitian microcavity lattice when an external light source is injected at a specific point. To ensure stability, we apply global damping to all microcavities, which shifts the entire spectrum downward along the imaginary axis. The system's evolution is governed by a Schrödinger-like equation:

$$i\partial_t\vec{\psi}(t) = H\vec{\psi}(t) + \vec{\psi}_0(t), \tag{1}$$

where $\vec{\psi}(t)$ is the system's state, H is the non-Hermitian Hamiltonian, and $\vec{\psi}_0(t)$ represents the external source. Our focus is on the steady-state solution of this equation, which describes the long-lived response of the system rather than the eigenstates of H.

The key observation is the "source-center offset" phenomenon. In conventional systems, wave packets propagate symmetrically from the external source location, akin to ripples in water spreading from where a stone is dropped. In contrast, our one-dimensional (1D) non-Hermitian lattice exhibits a wave packet emerging from a point offset from the physical injection position. This offset is not a topological invariant. It stems from the fact that the spectrum is encircling a finite region as the wavevector k varies[27, 28], which introduces directional phase accumulation in the complex energy spectrum. The offset magnitude can be controlled by tuning the source frequency. Extending this shift to 2-dimenional (2D) lattices, this mechanism generates frequency-dependent V-shaped propagation patterns, where the apex angle is dictated by the interplay between the injected light's frequency and the strength of the interchain's coupling.

II. CENTER-SOURCE OFFSET IN THE 1D NON-HERMITIAN MODEL.

We study a 1D microcavity lattice consisting of two sublattices, labeled by α and β[29–31]. The equation of motion is given by:

$$\begin{aligned} i\frac{d}{dt}\begin{pmatrix}\alpha_n(t)\\ \beta_n(t)\end{pmatrix} &= \begin{pmatrix} iR & R\\ R & -iR\end{pmatrix}\begin{pmatrix}\alpha_{n-1}(t)\\ \beta_{n-1}(t)\end{pmatrix} + \begin{pmatrix} i\Gamma_1 & V\\ V & i\Gamma_2\end{pmatrix}\begin{pmatrix}\alpha_n(t)\\ \beta_n(t)\end{pmatrix}\\ &+ \begin{pmatrix} -iR & R\\ R & iR\end{pmatrix}\begin{pmatrix}\alpha_{n+1}(t)\\ \beta_{n+1}(t)\end{pmatrix} + \begin{pmatrix} if(t)\delta_{nm}\\ if(t)\delta_{nm}\end{pmatrix}, \end{aligned} \tag{2}$$

where n indexes the unit cell, R and V denote the intercell and intracell couplings, respectively, and $\Gamma_{1(2)}$ represent the damping rates. The final term corresponds to an external point-like source located in the m-th unit cell, where $f(t)$ describes the temporal profile of the source. For simplicity, we assume $m = N/2$, positioning it at the system's center, and set the source frequency to ω_0, such that $f(t) = e^{-i\omega_0 t}$. The imaginary unit i on both sides of the equation ensures a Schrödinger-like structure.

A schematic of the model is shown in Fig. 1. After applying a Fourier transform, the equation of motion becomes:

$$\begin{aligned} i\frac{d}{dt}\begin{pmatrix}\alpha_k(t)\\ \beta_k(t)\end{pmatrix} &= \begin{pmatrix} 2R\sin k + i\Gamma_1 & V + 2R\cos k\\ V + 2R\cos k & -2R\sin k + i\Gamma_2\end{pmatrix}\begin{pmatrix}\alpha_k(t)\\ \beta_k(t)\end{pmatrix}\\ &+ \frac{ie^{-imk}}{\sqrt{N}}\begin{pmatrix} f(t)\\ f(t)\end{pmatrix}. \end{aligned} \tag{3}$$

* Corresponding author; xiongye@njnu.edu.cn

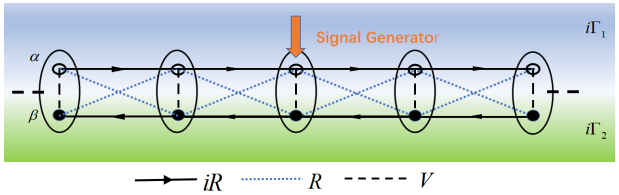

FIG. 1. Schematic of the 1D non-Hermitian micro-ring resonator lattice with nearest-neighbor couplings,The arrows denote the phase direction.

In the absence of an external source, H_k, which is the 2×2 matrix in Eq. (3), determines the eigenfrequencies and eigenstates. Depending on the parameters, the eigenfrequencies can either form two distinct bands or merge into a single unified band in the complex plane. The findings of this paper apply to both scenarios, and for simplicity, we focus on the latter case. As shown in Fig. 2, all eigenfrequencies lie below the real axis, indicating their decay over time and ensuring system stability. A color scheme distinguishes the dominant sublattice in the eigenstates, with red representing the α sublattice and blue representing the β sublattice.

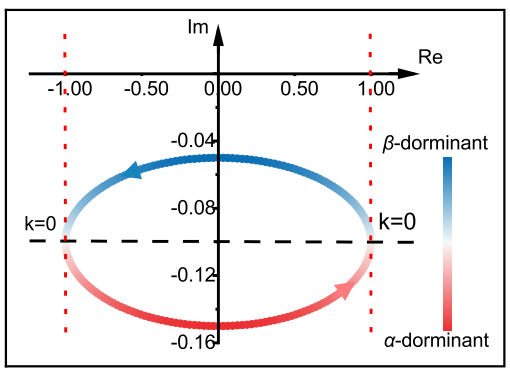

FIG. 2. Eigenfrequency spectrum for $\Gamma_1 = -0.05$, $\Gamma_2 = -0.15$, $V = 0.5$, and $R = 0.25$. Arrows indicate the frequency change direction with k.

We numerically solve the equation of motion, Eq. (2), using the fourth-order Runge-Kutta method on a chain of 100 units with periodic boundary conditions. The amplitude of the final state, which ceases to evolve over time, is depicted in Fig. 3. At $\omega_0 = -1.5$, the highest amplitude coincides with the source location (the 50th unit cell). However, for $\omega_0 = 0$ and -0.5, the peak amplitude shifts: on the α sublattice, it moves to the 51st unit cell, and on the β sublattice, it shifts to the 49th unit cell. This shift persists when $|\omega_0| < \Omega_0$, where $\Omega_0 = 1$ defines the range of the eigenspectrum along the real axis. Additionally, we observe that the shape of the wave packet exhibits a bias correlated with this shift.

To clarify the observed offset, we analyze the system's steady-state solution $\vec{\psi}$, which corresponds to the stationary solution of Eq. (3) after sufficient evolution time.

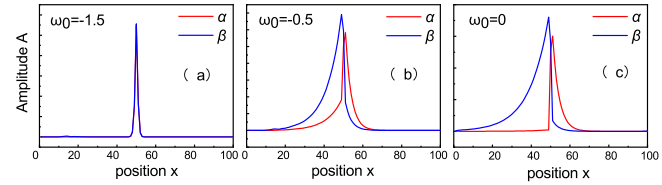

FIG. 3. Position-amplitude diagrams for different ω_0 at $t = 75$. Red and blue represent the α and β sublattices, respectively. The lattice parameters are the same as in Fig. 2.

To resolve ambiguities between momentum (k) and real-space (r) representations we employ Dirac's bra-ket notation $|k\rangle$ and $\langle\langle k|$ to denote the right and left eigenstates of H_k, The observed state is given by the real space projection $\vec{\psi} = \langle r|\psi\rangle$ of $|\psi\rangle$, which is

$$|\psi\rangle = \frac{1}{\omega_0 - H}|f\rangle = \sum_{ka} \frac{1}{\omega_0 - \epsilon_a(k)}|k_a\rangle\langle\langle k_a|f\rangle. \quad (4)$$

Here ϵ_a is the ath eigenvalue of H_k, $|f\rangle$ is the external driving term. The left and right eigenstates have the orthonormal relations: $\langle\langle k_a|k'_{a'}\rangle = \delta(k-k')\delta(a-a')$.

We show that the state $|\psi\rangle$ is expressed as a dual-space summation over both momentum k and band-index a, $|\psi\rangle = \sum_{ka} Y_a(k)\hat{Z}_a(k)|f\rangle$, where $Y_a(k) = \frac{1}{\omega_0 - \epsilon_a(k)}$ and $\hat{Z}_a = |k_a\rangle\langle\langle k_a|$. The summation over k corresponds to a real-space convolution after Fourier transform, as dictated by the convolution theorem. Notably, this formalism can be extended to the band-index space a by introducing an additional Fourier transform across bands, thereby converting the summation over a into another convolution. This approach is further motivated by the interconnected band structure of our model. The energy dispersion $\epsilon_a(k)$ and the eigenstates exhibit a periodicity of 4π, effectively doubling the Brillouin zone compared to the original 2π periodicity of H_k.

We introduce the q specified Wannier functions $|n_q\rangle$ and $|n_q\rangle\rangle$ as:

$$|n_q\rangle(|n_q\rangle\rangle) = \sum_{ka} e^{ikn} e^{iq(a-1)}|k_a\rangle(|k_a\rangle\rangle), \quad (5)$$

where $k \in (0, 2\pi)$ and q takes D discrete numbers in $(0, 2\pi)$ and D is the number of bands. This procedure implements sequential band alignment in the k space, ensuring the composite spectrum spans a total interval of $2\pi D$ without overlap. The sequential alignment optimizes the arrangement of individual bands to collectively occupy the extended $2\pi D$ range, preserving spectral continuity while avoiding aliasing artifacts.

The observed state $|\psi\rangle$ is

$$|\psi\rangle = \sum_{nq} Y_{-q}(-n)\hat{Z}_q(n)|f\rangle, \quad (6)$$

where $\hat{Z}_q(n) = \sum_{n'q'} |(n'+n)_{q'+q}\rangle\langle\langle n'_{q'}|$. Because $\hat{Z}_q(n)\hat{Z}_{-q}(-n) = \hat{1}$, the offset matrix $\hat{X}_q(n)$ which is defined by $\sum_k e^{ik\hat{X}_q(n)} = \hat{Z}_q(n)$ will change sign as $q \to -q$

and $n \to -n$ simultaneously. The universality of this property is preserved irrespective of the Hermitian nature of the Hamiltonian H_k.

Here we present the analysis of three demo cases for $\epsilon_a(k)$. The first one is that a hermitian Hamiltonian, where $\epsilon_a(k)$ resides strictly on the real axis. This ensures that $Y_a(k)$ is a real-valued function in both k and a space. This reality condition enforces the symmetry: $Y_q(n)$ is an even function in both Fourier-transformed q and n spaces. Consequently, such systems inherently suppress spectral offsets due to the absence of complex interference or asymmetric energy contributions. The second case involves $\epsilon_a(k)$ encircling ω_0 in the complex plane, satisfying $\frac{1}{\omega_0-\epsilon_a(k)} = e^{ik}$. After Fourier transformation, $Y_q(n) = \delta(n+1)\delta(q)$. This indicates that all components of $|\psi\rangle$ offset one unit cell to the right relative to $|f\rangle$. However, this lattice becomes dynamically unstable due to the emergence of exponentially growing eigenstates. The third case aligns with the model studied in this paper. At first glance, the absence of spectral winding (i.e., $\epsilon(k)$ does not encircle ω_0) suggests no offset should occur. However, when approximating the spectrum as a circle of radius R_0 centered at O in the complex plane, the terms $Y_1(k) = \frac{1}{\omega_0-O-R_0e^{ik/2}}$ and $Y_2(k) = \frac{1}{\omega_0-O+R_0e^{ik/2}}$ introduce asymmetry in k space. This asymmetry propagates to $Y_q(n)$ via Fourier transformation, breaking symmetry in q and n spaces and enabling the offset. The strength of the asymmetry diminishes as $|\omega_0 - O|$ increases. Consequently, when $\omega_0 = -1.5$ (far from O), no offset is observed, despite the residual non-Hermitian nature of H_k.

The offset phenomenon, while not a strict topological invariant due to its dependence on the detailed spectral geometry (e.g., the components of $Y_q(n)$), is strongly tied to how rapidly spectrum encircles the point gap. A higher encircling rate enhances the phase gradient in $Y_a(k)$, dominating higher-order terms in $Y_q(n)$. For instance, doubling the encircling rate in a model with next-nearest-neighboring hoppings leads to a doubled offset.

The offset can also be intuitively understood by analyzing the sublattice-resolved spectral evolution in Fig. 2. For the first band, the spectrum rotates anticlockwise around ω_0 roughly, while the second band rotates clockwise. Crucially, the two bands exhibit sublattice imbalance: the first band is dominated by the α sublattice component, and the second band by the β sublattice. When the response state ψ is projected onto each sublattice separately, these opposite winding directions induce oppositely directed offsets for α and β.

III. IN THE TWO-DIMENSIONAL NON-HERMITIAN LATTICES.

The above research has shown that, under specific conditions in a 1D chain, the center of the response wave packet produced by external driving may not coincide with the source position. This intriguing behavior prompts the inquiry: What will be the system's dynamics when multiple such chains are arranged in parallel and weak couplings are introduced between the adjacent chains?

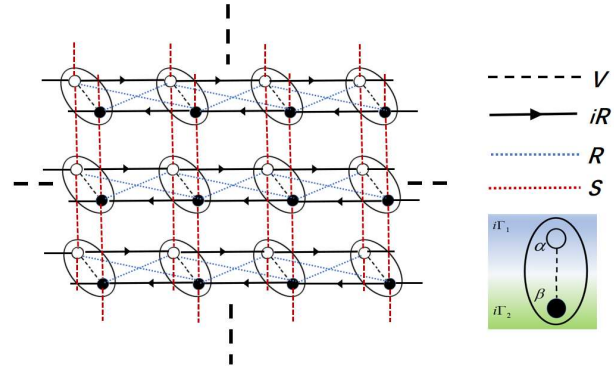

FIG. 4. Two-dimensional non-Hermitian composite micro-ring resonator array with nearest-neighbor couplings.

We establish a two-dimensional non-Hermitian square micro-ring resonator array, as depicted in Fig. 4. The equation of motion reads

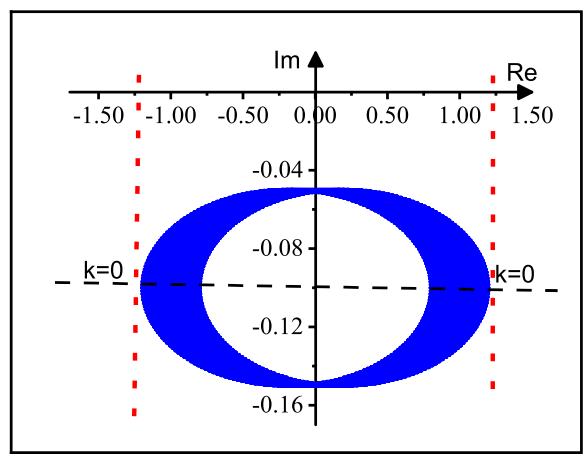

FIG. 5. The eigenfrequency spectrum for $\Gamma_1 = -0.05$, $\Gamma_2 = -0.15$, $V = 0.5$, $R = 0.25$ and ω_0=-0.5.

$$
\begin{aligned}
i\frac{d}{dt}\begin{pmatrix}\alpha_{n_x,n_y}(t)\\ \beta_{n_x,n_y}(t)\end{pmatrix} &= \begin{pmatrix} i\Gamma_1 & V \\ V & i\Gamma_2\end{pmatrix}\begin{pmatrix}\alpha_{n_x,n_y}(t)\\ \beta_{n_x,n_y}(t)\end{pmatrix} \\
&+ \begin{pmatrix} -iR & R \\ R & iR\end{pmatrix}\begin{pmatrix}\alpha_{n_x+1,n_y}(t)\\ \beta_{n_x+1,n_y}(t)\end{pmatrix} + \begin{pmatrix} iR & R \\ R & -iR\end{pmatrix}\begin{pmatrix}\alpha_{n_x-1,n_y}(t)\\ \beta_{n_x-1,n_y}(t)\end{pmatrix} \\
&+ \begin{pmatrix} S & 0 \\ 0 & S\end{pmatrix}\begin{pmatrix}\alpha_{n_x,n_y\pm1}(t)\\ \beta_{n_x,n_y\pm1}(t)\end{pmatrix} + \begin{pmatrix} if(t)\delta_{xx_0}\delta_{yy_0} \\ if(t)\delta_{xx_0}\delta_{yy_0}\end{pmatrix}
\end{aligned}
\tag{7}
$$

Here, n_x and n_y denote the indices of the unit cells on the 2D lattice. The hopping terms along the x-axis and the on-site damping rates are identical to those in the

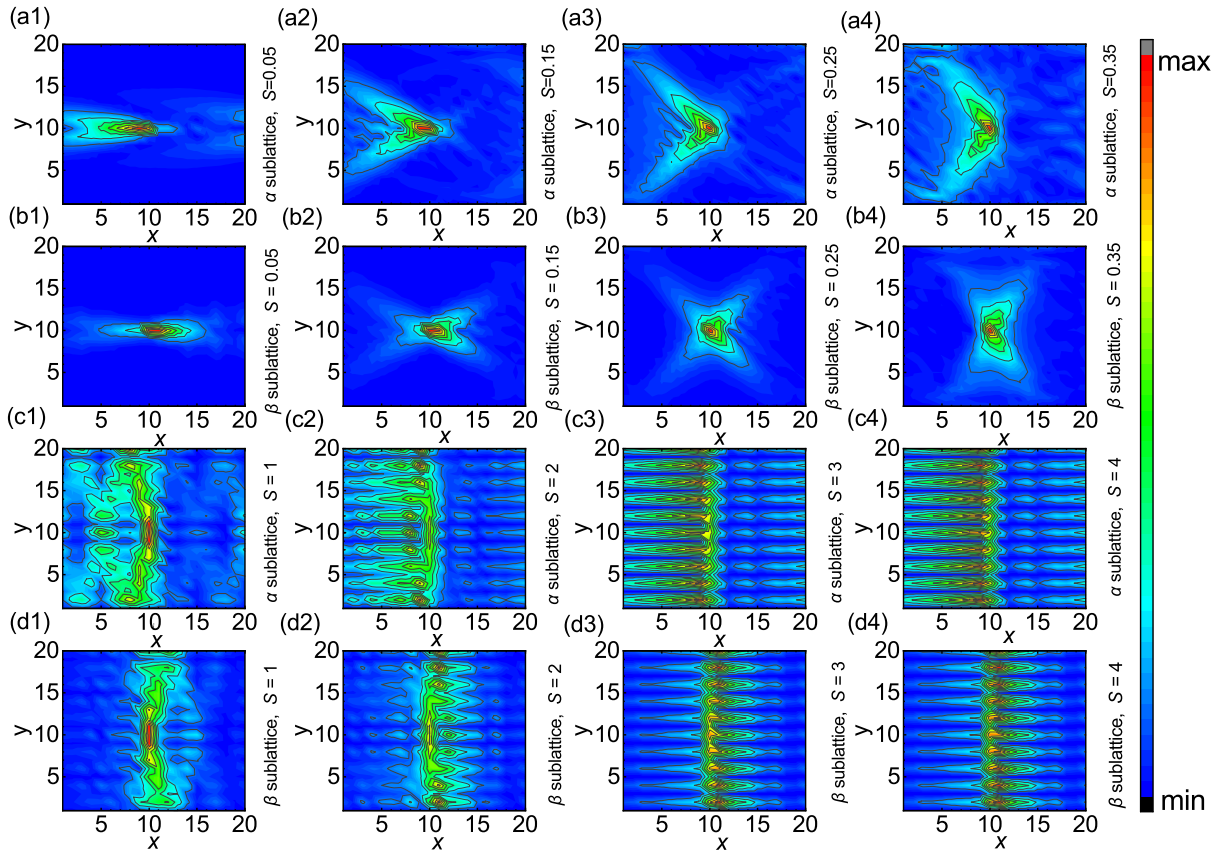

FIG. 6. At $t = 50$, the amplitude of the excited wave packet on the 2D lattice. The parameters of the lattice are the same as that in Fig. 2. $\omega_0 = -0.5$.

1D case. The parameter S represents the strength of the hopping along the y-axis between adjacent sites. An external source is located at (n_{x_0}, n_{y_0}), which is at the center of the 2D lattice in our study.

Applying a Fourier transform to the wave vector space (k_x, k_y), we derive the time-evolution equations for the system at each (k_x, k_y), $i\frac{d}{dt}\binom{\alpha_{k_x,k_y}(t)}{\beta_{k_x,k_y}(t)} = H_{k_x,k_y}\binom{\alpha_{k_x,k_y}(t)}{\beta_{k_x,k_y}(t)} + \frac{ie^{-ix_0k_x}e^{-iy_0k_y}}{\sqrt{N_xN_y}}\binom{f(t)}{f(t)}$. This process yields the dynamical matrix H_{k_x,k_y} in k-space,

$$H = \begin{pmatrix} U_1 & V + 2R\cos k_x \\ V + 2R\cos k_x & U_2 \end{pmatrix}, \tag{8}$$

where $U_{1(2)} = \pm 2R\sin k_x + 2S\cos k_y + i\Gamma_{1(2)}$.

The spectrum of the Hamiltonian H_{k_x,k_y} is given by $\omega_{k_x,k_y} = 2S\cos k_y + \frac{i(\Gamma_1+\Gamma_2)}{2} \pm\sqrt{\left(2R\sin k_x + \frac{i(\Gamma_1-\Gamma_2)}{2}\right)^2 + (V + 2R\cos k_x)^2}$, and is illustrated schematically in Fig. 5. The system remains stable, as all spectral components lie below the real axis.

To solve the system comprising 20×20 unit cells subject to periodic boundary conditions, the fourth-order Runge-Kutta numerical method is utilized. This approach yields numerical solutions for the complex amplitudes at each micro-ring cavity at every time step, thereby ensuring precise tracking of the system's temporal evolution.

We observe that the α (β) component of the wave packet spreads asymmetrically from the center, creating a distinct V-shaped pattern as illustrated in Fig. 6. Notably, the angle of this V is modulated by the magnitude of the coupling parameter S.

The anomalous transport observed in the 2D lattice can be attributed to the positional offset mechanism inherent in individual 1D chains. When the interchain coupling strength S is sufficiently weak, the 2D lattice can be approximated as a superposition of weakly coupled 1D chains. By localizing a delta-function external source with driving frequency ω_0 at the system center, the dynamics of the central chain directly inherits the 1D behavior. For $|\omega_0| < \Omega_0$ (where Ω_0 marks the critical frequency threshold), the excited wavepacket in the α-sublattice undergoes a left positional shift of one unit cell along the chain direction, while the β-sublattice exhibits an opposite offset with less pronounced strength. Adjacent chains become activated through nearest-neighbor coupling to the central chain. The external excitation in these secondary chains comes from the excited state on the central chain and inherits the shifted position.

They will subsequently induce an additional positional offset. This cascading displacement propagates radially outward, generating a characteristic V-shaped wavefront trajectory originating from the driven central site. The enhanced anomalous transport in the α-sublattice compared to the β-sublattice arises from fundamental differences in $\frac{1}{\omega_0-\epsilon_\alpha(k)}$ for the two bands. The peak for β-sublattice in Fig. 3 is lower than that of α-sublattice, indicating stronger damping in the sublattice. Consequently, the β-sublattice excitation demonstrates reduced spatial coherence, rendering its V-shaped trajectory less distinguishable compared to the sharp propagation signature of the α-sublattice. When $|\omega_0| > \Omega_0$, the offset mechanism in the 1D chains disappear, as does the V-shaped wavefront trajectory.

For strong interchain coupling, the previously described transport scenario breaks down. A representative case at $S = 4$ demonstrates that the wave morphology undergoes a marked transformation. Specifically, the externally driven excitation at the system center exhibits anisotropic propagation: it propagates preferentially along the vertical axis while retaining the characteristic behavior of the 1D chain in the horizontal direction. This phenomenon arises from the dominance of interchain hybridization over intrachain dispersion when S exceeds the critical coupling strength.

IV. CONCLUSIONS.

This study establishes a micro-resonator arrays to present non-equilibrium steady-state dynamics in non-Hermitian systems under coherent excitation, where results unveil transport anomalies: wavepacket displacement offset in 1D lattices and V-shaped wavefront propagation in 2D geometries.

Previous research on transport in non-Hermitian systems has predominantly focused on the unbalanced evolution of distinct eigenstates. However, our findings provide fresh perspectives on response dynamics within these systems. Notably, while the offset itself is not a topological invariant, the proposed mechanism allows for direct estimation of the rate of spectral evolution in the complex plane. This offers a novel approach to understanding and analyzing transport phenomena in non-Hermitian systems.

In practical applications, our work provides a methodology for elucidating the spectral structure on the complex plane. Moreover, the fundamental mechanism we uncover can be applied to obfuscate the source location, enabling applications in diverse domains such as signal processing and wavefront-engineering. For example, these lattice configurations enable the separation of the dual modes in an injected signal at specific frequencies.

ACKNOWLEDGMENTS

This work was supported by the National Foundation of Natural Science in China Grant No. 10704040.

[1] C. M. Bender and S. Boettcher, Phys. Rev. Lett. **80**, 5243 (1998).
[2] L. Feng, R. El-Ganainy, and L. Ge, Nature Photonics **11**, 752 (2017).
[3] R. El-Ganainy, K. G. Makris, M. Khajavikhan, Z. H. Musslimani, S. Rotter, and D. N. Christodoulides, Nature Physics **14**, 11 (2018).
[4] S. K. Ozdemir, S. Rotter, F. Nori, and L. Yang, Nature Materials **18**, 783 (2019).
[5] M.-A. Miri and A. Alù, Science **363**, 7709 (2019), https://www.science.org/doi/pdf/10.1126/science.aar7709.
[6] V. DeGiorgio and M. O. Scully, Phys. Rev. A **2**, 1170 (1970).
[7] F. Xie, M. Ren, W. Wu, D. Yu, W. Cai, and J. Xu, Phys. Rev. Lett. **125**, 237401 (2020).
[8] M. Berry, Czechoslovak Journal of Physics **54**, 1039 (2004).
[9] W. D. Heiss, Journal of Physics A: Mathematical and General **37**, 2455 (2004).
[10] W. D. Heiss, Journal of Physics A: Mathematical and Theoretical **45**, 444016 (2012).
[11] Z.-P. Liu, J. Zhang, i. m. c. K. Özdemir, B. Peng, H. Jing, X.-Y. Lü, C.-W. Li, L. Yang, F. Nori, and Y.-X. Liu, Phys. Rev. Lett. **117**, 110802 (2016).
[12] E. J. Bergholtz, J. C. Budich, and F. K. Kunst, Rev. Mod. Phys. **93**, 015005 (2021).
[13] Y. Xiong, Journal of Physics Communications **2**, 035043 (2018).
[14] S. Yao and Z. Wang, Phys. Rev. Lett. **121**, 086803 (2018).
[15] K. Yokomizo and S. Murakami, Phys. Rev. B **104**, 165117 (2021).
[16] Z. Yang, K. Zhang, C. Fang, and J. Hu, Phys. Rev. Lett. **125**, 226402 (2020).
[17] J.-W. Ryu, Phys. Rev. A **108**, 052205 (2023).
[18] C. Caloz, A. Alù, S. Tretyakov, D. Sounas, K. Achouri, and Z.-L. Deck-Léger, Phys. Rev. Appl. **10**, 047001 (2018).
[19] S. Longhi, D. Gatti, and G. D. Valle, Scientific Reports **5**, 13376 (2015).
[20] S. Longhi, Phys. Rev. B **103**, 054203 (2021).
[21] T. Orito and K.-I. Imura, Phys. Rev. B **105**, 024303 (2022).
[22] Y.-M. R. Hu, E. A. Ostrovskaya, and E. Estrecho, Phys. Rev. B **108**, 115404 (2023).
[23] E. M. Graefe and R. Schubert, Phys. Rev. A **83**, 060101 (2011).
[24] E. Poli, A. Bottino, D. Korger, O. Maj, F. Palermo, and H. Weber, New Journal of Physics **26**, 013016 (2024).
[25] B. Alon, R. Ilan, and M. Goldstein, Phys. Rev. B **110**, 245103 (2024).
[26] D. Braghini, *Stability and Performance of Non-Reciprocal Metastructures Exhibiting the Non-Hermitian Skin Effect*, Ph.D. thesis, [sn] (2024).

[27] J. Claes and T. L. Hughes, Phys. Rev. B **103**, L140201 (2021).
[28] L. Li, S. Mu, C. H. Lee, and J. Gong, Nature communications **12**, 5294 (2021).
[29] J. Heebner, R. Grover, and T. Ibrahim, *Optical microresonator theory* (Springer, 2008).
[30] B. Peng, Ş. K. Özdemir, F. Lei, F. Monifi, M. Gianfreda, G. L. Long, S. Fan, F. Nori, C. M. Bender, and L. Yang, Nature Physics **10**, 394 (2014).
[31] F. Zhang, Y. Feng, X. Chen, L. Ge, and W. Wan, Physical review letters **124**, 053901 (2020).